ACS MATERIALS LETTERS

www.acsmaterialsletters.org

LETTER

Incorporating Dopant Effects in the Plasmon Ruler for Metal-Oxide Nanocrystal Superlattices

M. Wren Berry, Allison M. Green, Benjamin J. Roman, Thomas M. Truskett,* and Delia J. Milliron*

Cite This: *ACS Materials Lett.* 2024, 6, 1929–1937

Read Online

ACCESS | Metrics & More | Article Recommendations | Supporting Information

ABSTRACT: Plasmonic nanocrystals in close-packed assemblies exhibit collective optical resonance and strongly concentrated electric fields due to coupling. The spectral red-shift from the localized surface plasmon resonance (LSPR) of isolated nanocrystals to that of an assembly reflects coupling strength, which depends on nanocrystal characteristics and assembly structure. Scaling laws that relate these shifts to nanocrystal spacing are useful to systematically describe plasmon coupling and predict peak shifts for materials design. Here, we develop a unified scaling relationship that accounts for unique properties of metal-oxide plasmonic nanocrystals by considering the dopant influence on the LSPR frequency and free electron distribution within nanocrystals. We propose a rescaled plasmon ruler, adjusted for the presence of a dopant-dependent depletion layer, to describe the spectral shifts of colloidal indium tin oxide nanocrystals assembled into close-packed superlattices. This framework can guide designs of plasmonic materials to realize specific optical characteristics based on synthetically controllable attributes of nanocrystal building blocks.

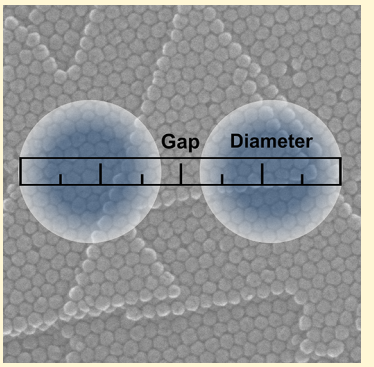

Colloidal nanocrystal (NC) superlattices, which are densely packed assemblies with long-range periodic ordering, have optoelectronic properties dictated by the properties of the constituent NCs and interactions arising from the close proximity of NC building blocks.[1−3] Plasmonic NCs interact strongly with light through localized surface plasmon resonance (LSPR) that induces a large oscillatory dipole in each NC.[4,5] When assembled into multiparticle superstructures, the excitation of LSPR in each NC mutually polarizes the surrounding NCs, hybridizing their localized modes into collective plasmon resonance (CPR) modes.[6−8] The strength of these plasmon coupling effects is reflected in the magnitude of spectral shift of the hybridized modes from the LSPR of the isolated NCs.[8−12] In this work, we elucidate systematic trends in plasmon coupling strength as it depends on characteristics of assembled plasmonic metal-oxide NCs by evaluating the spectral redshifts from isolated NC LSPR to CPR of superlattice assemblies.

Previously, plasmonic shift from isolated nanoparticles to the longitudinal mode of coupled dimers has been related to the distance between the nanoparticles, where increasing space between nanoparticles causes the plasmon shift to decay approximately exponentially.[8,9,11,13] This relationship allows the interpretation of the LSPR spectrum, observable in the far-field, to approximately "measure" nanoscopic spacing between particles. Studies of coupled pairs of metallic particles led to plasmon ruler scaling laws that indicate an empirical decaying exponential trend between the shift of the LSPR wavelength along the interparticle axis, scaled by the initial LSPR peak position, and particle spacing, described by the ratio of the gap between particles to their diameter.[13−15] This concept has been generalized to extended noble-metal nanoparticle assemblies, like silver (Ag) and gold (Au) nanoparticle superlattices.[16−19] In these close-packed structures, each particle's LSPR is coupled to many nearby polarizations, causing the decay lengths in superlattice plasmon rulers to be longer range than for particle pairs.[16−19] The spectral shift is an indication of LSPR coupling strength and, as we recently highlighted, is predictive of the intensity of the near-field enhancement in the local hot spots.[20] So, evaluating trends in spectral shifts with superlattice structure and nanoparticle properties is a useful strategy for creating materials to achieve targeted optical properties, including both far-field spectral characteristics and near-field enhancements. Plasmonic nanoparticle-based materials can thereby be customized for specific

Received: January 29, 2024
Revised: April 5, 2024
Accepted: April 8, 2024
Published: April 11, 2024

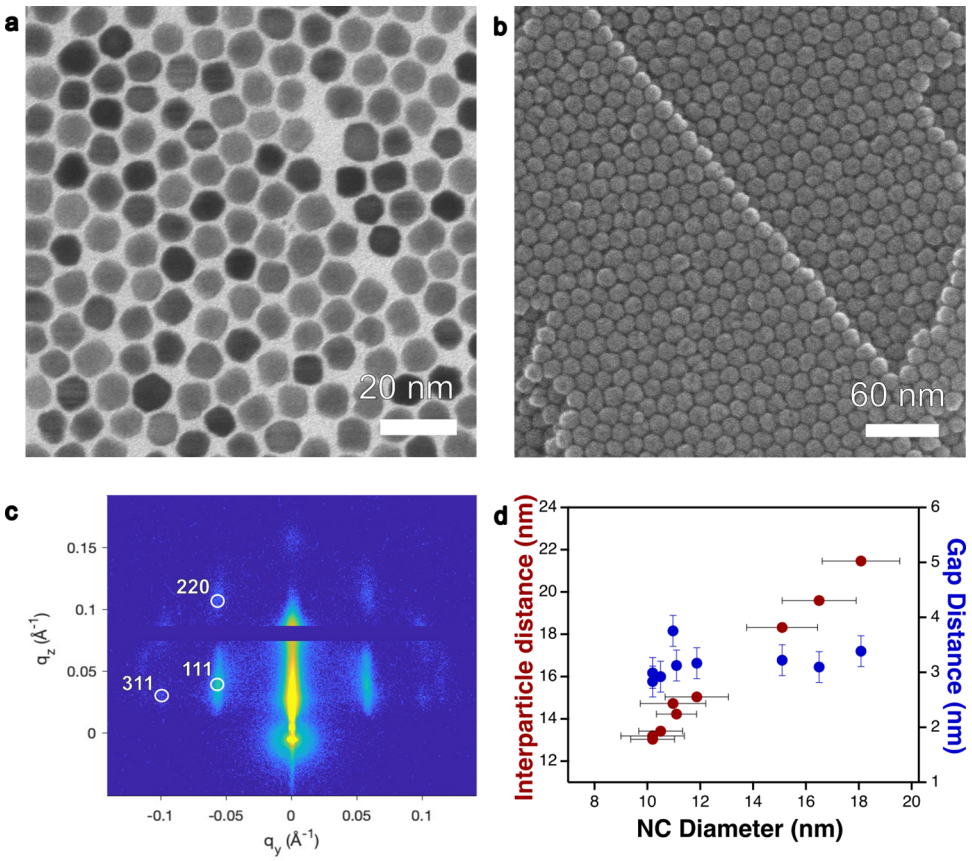

Figure 1. NC and superlattice structural characterization. (a) STEM image of 18 nm 5% Sn ITO NCs. (b) SEM image of a three-dimensional (3D) superlattice of 18 nm 5% Sn ITO NCs. (c) GISAXS pattern of a superlattice of 12 nm 5% Sn ITO; peaks are indexed according to the FCC lattice structure. (d) Interparticle (center-to-center) distances and calculated gap distances between NC surfaces for each superlattice analyzed. Error bars indicate the standard deviation in diameter for each NC sample and the standard deviation of all gap distances.

applications such as surface-enhanced spectroscopies, radiative cooling, and photonic devices.[21−26] While the principles governing plasmonic coupling between noble-metal nanoparticles have been explored for decades, plasmonic semiconductor NCs have emerged more recently as highly tunable optical components.

Doped metal-oxide NCs exhibit LSPR in the near-infrared (IR) region. Unlike conventional metallic nanoparticles, which have a relatively fixed free electron concentration, doping concentration of the metal-oxide NCs can be tuned synthetically, to vary the free electron concentration and therefore the frequency of their LSPR.[2,5,27] In tin (Sn)-doped indium oxide (ITO) NCs, for example, the Sn concentration tunes the LSPR frequency across the IR region, decoupling the resonance wavelength from NC size and shape.[28,29] While LSPR coupling has been studied in lithographically patterned ITO nanorod arrays and isolated pairs of ITO NCs,[30−33] the influence of Sn doping concentration on coupling remains to be elucidated. Here, we address this gap by analyzing spectroscopic shifts when assembling ITO NCs of varying size and dopant concentration (% Sn) into superlattices.

By extending the concept of the plasmon ruler to ITO NC superlattices, we illuminate the influence of dopants on the plasmon coupling strength. The primary effect of dopants in tuning the LSPR frequency is naturally described by the original concept of the plasmon ruler, where the spectral shift is scaled relative to the initial frequency (or wavelength). However, the universal scaling fails to predict differences in coupling between NCs with different % Sn in structurally similar superlattices, which persist even after scaling. This limitation is resolved by considering the influence on LSPR coupling of near-surface depletion layers, which are known to occur in doped metal-oxide NCs and impact individual NC optical properties.[29,34−36] Here, we show that depletion layers and their dependence on dopant concentration strongly perturb plasmon coupling. To account for these effects, we propose a rescaled, dopant-dependent plasmon ruler that effectively describes the scaling of plasmon peaks with ITO NC superlattice structure and can be used to predict superlattice properties for design.

Regular morphology and size uniformity of NCs are vital to assembling consistently ordered superlattices. ITO NCs were synthesized with an established slow-growth synthetic method that offers precise control over % Sn and NC size. The NCs produced by this synthesis are capped with oleate ligands and exhibit approximately isotropic interactions and ideal solvent dispersibility.[37−40] Regular, quasi-spherical morphology of the NCs was confirmed using bright-field scanning transmission electron microscopy (STEM) and small-angle X-ray scattering (SAXS) of dilute NC dispersions (see Figure 1a, as well as Figures S1 and S2). The size and polydispersity of the NCs were evaluated by fitting SAXS patterns for dilute NC dispersions with a spheroid form factor; size dispersity was less than 10% for all samples studied (Figure S3 and Table S1). Superlattices were assembled by slow evaporation of toluene, depositing ordered films onto angled undoped silicon

https://doi.org/10.1021/acsmaterialslett.4c00220
ACS Materials Lett. 2024, 6, 1929−1937

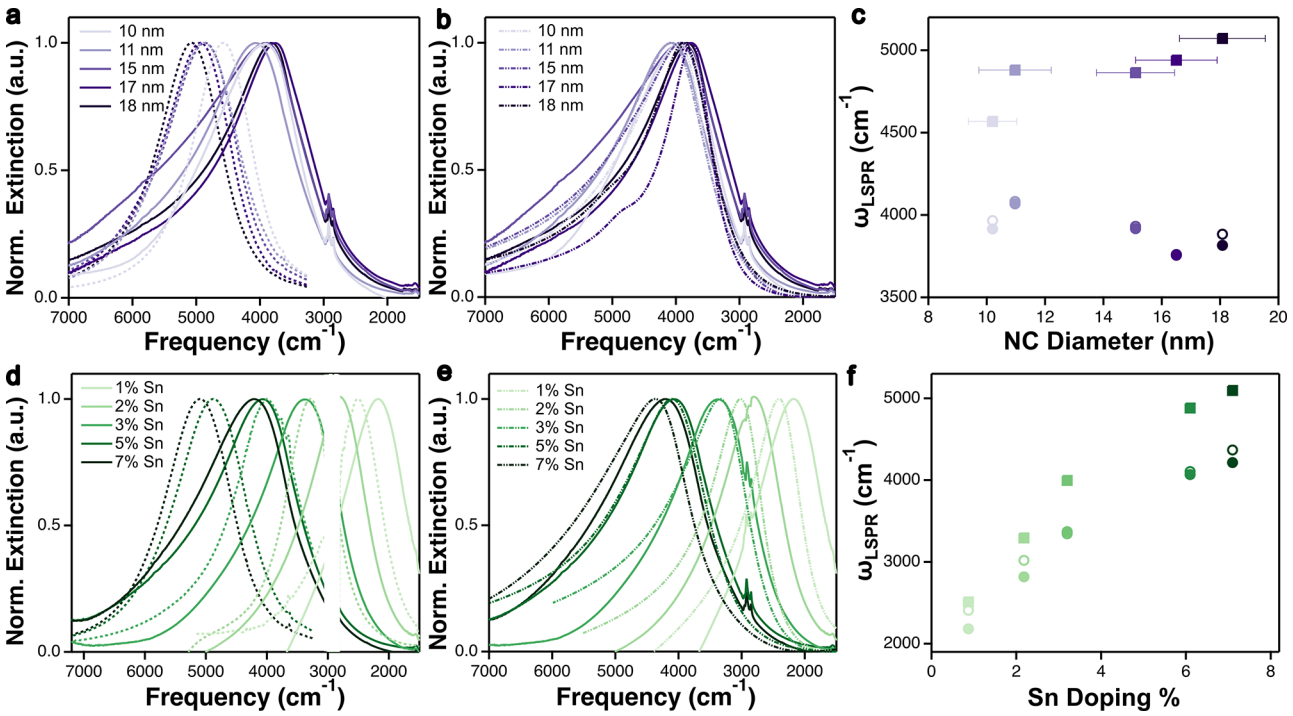

Figure 2. Plasmon coupling trends related to NC characteristics. Extinction spectra for dispersions (dashed) and superlattices (solid) of (a) varying size NCs and (d) varying % Sn NCs, where regions exhibiting intense ligand vibrational peaks have been omitted for clarity. Experimental superlattices (solid) and EMT-predicted (dotted-dashed) extinction spectra of (b) varying size NCs and (e) varying % Sn NCs. Extinction peak positions for dispersions (squares) and superlattices (circles; filled are experiments, open are EMT predictions) of (c) varying size NCs and (f) varying % Sn doped NCs. Error bars indicate polydispersity in size (c) and uncertainty in % Sn, which is less than the size of the markers (f). EMT predictions employ a core−shell Drude dielectric function reflecting an NC depletion layer (see the Methods section in the Supporting Information).

substrates. Following literature protocols, the initial concentrations of NC dispersions were ∼0.5 mg/mL and complete evaporation occurred after ∼10 days at 45 °C.[41,42] Resulting superlattice films ranged from 120 to 600 nm (Table S2 and Figure S4a) in thickness between samples. The large range of thickness was assumed to have little effect on coupling strength based on finite element simulations carried out with COMSOL showing minimal change in spectral peak position and line shape with superlattice thickness (see Figures S4b and S5), a result previously observed in Ag supercrystals.[3] The regular ordering of NCs in the superlattices was apparent by scanning electron microscopy (SEM), where a hexagonal packing pattern was seen in top-down imaging and cross-sectional imaging revealed close packing throughout the film thickness (Figures 1b, S1, S2, and S4a). To better assess the order throughout the film thickness and across macroscopic distances, scattering patterns were collected by grazing incidence SAXS (GISAXS).

The packing of ITO superlattices was determined from their GISAXS patterns, where the spacing between indexed peaks was used to calculate interparticle distances.[43] All superlattice samples showed GISAXS peaks indicative of face-centered cubic (FCC) ordering, consistent with other reports of spherical nanocrystals functionalized with oleate ligands (see Figure 1c, as well as Figures S1 and S2).[44,45] The center-to-center interparticle distances between NCs in the assembled superlattices were calculated from the magnitudes of the observed Q_z and Q_y values of the two (111) peaks, converted to real space to find the close-packed interparticle distance (D) for an FCC lattice by $(2\pi/\sqrt{Q_z^2 + Q_y^2})\sqrt{3/2} = D$. The gap distance was then calculated by subtracting the NC diameter (determined from SAXS) from D. Gap distance in superlattices can vary with ligand density and interdigitation, which is dependent on the choice of ligand and solvent.[44,46] Considering the consistent surface chemistry and moderate radius of curvature of our NCs, we expect a uniform gap distance templated by the oleate ligands; the average gap found by GISAXS analysis is 3.17 nm ± 0.3 nm (Figure 1d and Table S3), which is approximately twice the solvent-swollen oleate ligand shell thickness previously measured using SAXS and small-angle neutron scattering.[39,47,48] With the gap distance being constant across our samples, because of the oleate ligand, we vary the NC diameter to examine the impact of the *relative* gap on plasmon coupling.

We hypothesized that larger ITO NCs would give rise to stronger plasmon coupling and larger spectral shifts, similar to previously reported trends for Au and Ag nanoparticles.[49,50] Larger NCs with a constant, small gap due to surface ligands experience stronger electric field interactions arising from dipoles on neighboring NCs, leading to more intense near and far field plasmonic interactions.[28,51−53] Here, a series of 5.5% ± 0.4% Sn ITO NCs were synthesized with diameters ranging from 10 nm to 18 nm to isolate the effects of NC size on plasmon coupling (Table S1). Each NC sample was used to prepare a superlattice, and optical spectra of each assembly were compared to the corresponding isolated, solvent-dispersed NCs to investigate the plasmon coupling. Each superlattice shows the characteristic redshift of the CPR, with greater shifts for larger NCs, indicating stronger LSPR coupling (Figure 2a). The lineshapes were also noticeably broadened upon assembly, which may arise due to plasmon

https://doi.org/10.1021/acsmaterialslett.4c00220
ACS Materials Lett. 2024, 6, 1929−1937

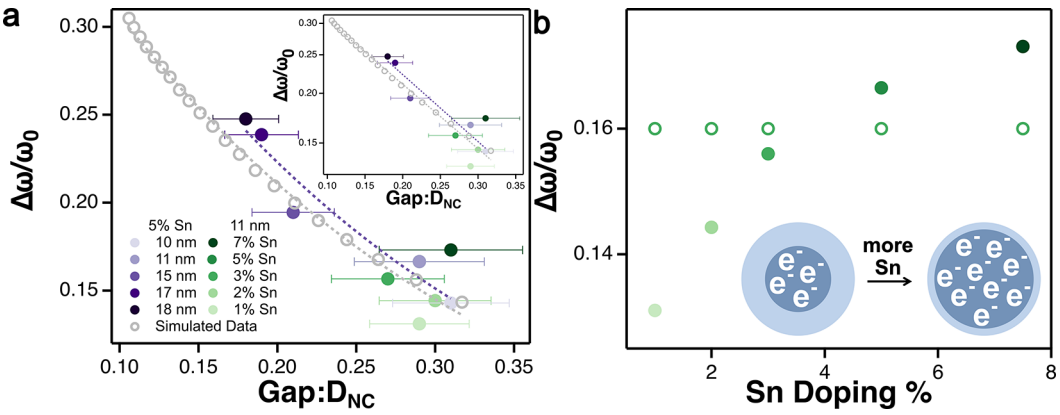

Figure 3. Evaluating the plasmon ruler scaling of ITO NC superlattices. (a) Experimental data plotted as a simple plasmon ruler paired with EMT predictions extending past the experimental data range and fitted with an exponential function. Experimental (size series only) fit parameters: A = 0.48 and ρ = 0.26, EMT fit parameters: A = 0.45 and ρ = 0.27. Inset shows a semilog plot. (b) Relative spectral shift observed experimentally (closed circles) and predicted by EMT (open circles). Scheme (inset) shows how the electron distribution changes with Sn doping. EMT predictions employ a Drude dielectric function with constant damping (see the Methods section in the Supporting Information).

coupling or from physical defects like cracks, where the coupling environment and optical resonances differ from the bulk of the superlattice.[54]

We anticipated that the magnitude of the spectral shift would increase with the LSPR frequency of the NCs. The LSPR of doped metal-oxide NCs may be tuned independent of size by varying the concentration of dopants incorporated during synthesis, which has no direct analogue in noble-metal nanoparticles; how dopant concentration affects plasmon coupling in assemblies is yet to be systematically investigated. To this end, a series of ITO NCs ranging from 1% to 7% Sn, all having diameters of 10.9 ± 0.6 nm, were synthesized and assembled into superlattices. As for the size series, the CPR is consistently red-shifted from the LSPR of the corresponding dispersed NCs (Figure 2d). The shift was found to grow monotonically with Sn % (Figure 2f), a trend previously observed in films of 6 nm ITO NCs and monolayer superlattices of 31 nm ITO NCs.[55,56] An increase in % Sn leads to stronger plasmonic coupling since the higher electron concentration results in stronger polarization of each NC and more intense electric fields that mediate their interactions.

To more deeply understand the trends in plasmonic coupling, we calculated the predicted optical response for each experimental superlattice using effective medium theory (EMT; see Figure 2b and 2e). The ingredients of an EMT calculation include a model for the dielectric properties of the NCs, an approximate method for accounting for the NC volume fraction and possibly interparticle correlations in the superlattice, and a film model. We treat the NCs as spheres with a plasmonic core and dielectric shell (see the Methods section in the Supporting Information) to reflect the presence of a depletion layer and use the (GI)SAXS-derived NC size and assembled FCC structure to fix the lattice volume fraction. The NC electronic structure model used here was informed by fitting extinction spectra of dilute nanocrystal dispersions with the heterogeneous ensemble Drude approximation (HEDA),[29] which accounts for ensemble heterogeneity and assumes a core−shell NC to model surface depletion layers (Figure S6 and Table S4). To estimate the effective dielectric function of the NC superlattice, either Maxwell−Garnett theory[57−59] or the three-point approximation of Torquato[60] offer potentially suitable approximations. Maxwell−Garnett theory provides an exact accounting of the contributions of dipoles to the optical response of a perfect FCC lattice at a given NC volume fraction. The approach from Torquato approximately accounts for multipolar contributions as well by incorporating information about three-point structural correlations in the perfect FCC lattice.[61,62] The three-point approximation has previously been observed to provide more accurate predictions for gold and silver nanoparticle assemblies than the Maxwell−Garnett approximation, while modestly overestimating multipolar contributions.[63] We found that the three-point approximation better reproduced the experimentally observed spectral shifts here and also predicted the observed asymmetric broadening of the superlattice spectra (Figures S7 and S8). This agreement may reflect the importance of multipolar interactions arising from the large volume fractions and substantial particle polarizabilities in our superlattices.

The three-point approximation yields an effective dielectric function that determines a frequency-dependent extinction coefficient, which can be used to predict absorption losses as light passes through the film. To more accurately model the experimental spectra, reflections occurring at the top and bottom interfaces of the film can be taken into account, following the general transfer matrix methodology.[64] Here, we use the transfer matrix method for a three-layer system consisting of semi-infinite air, a thin film, and a thick silicon substrate, which most closely represents the experimental system compared to alternate approaches we considered (see the Supporting Information). Film thicknesses for each experimental sample from cross-sectional SEM images were used as model inputs. Close agreement of the superlattice CPR peak frequencies and lineshapes between predictions and experiments is observed, which validates the core−shell model for the surface-depleted plasmonic NCs and the use of the three-point approximation paired with a transfer matrix model to understand trends in the optical response of these assemblies (Figures 2b and 2e). Asymmetric, broadened spectra are found even though the model presumes defect-free lattices of identical NCs, demonstrating the inherent role of coupling in establishing the lineshapes. The increasing magnitude of spectral shift for larger NCs (Figure 2c) qualitatively extends the well-established relationship between nanoparticle size and plasmon coupling observed for noble-

https://doi.org/10.1021/acsmaterialslett.4c00220
ACS Materials Lett. 2024, 6, 1929−1937

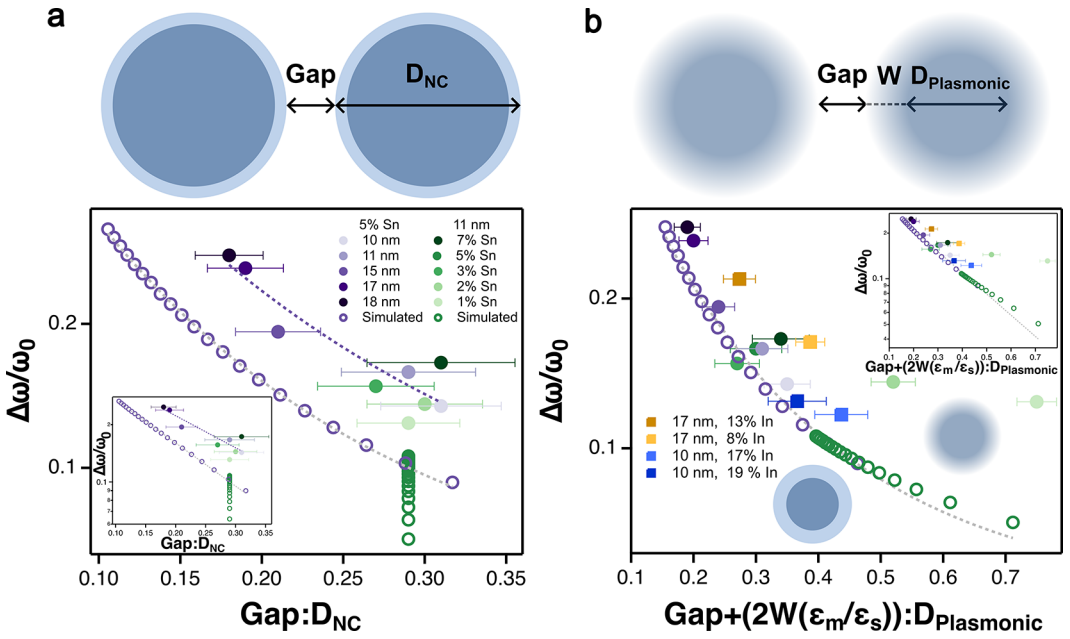

Figure 4. Plasmon ruler rescaled for depletion. (a) Schematic showing how gap:diameter ratio is represented in NC assemblies, where D_{NC} is the summation of the plasmonic core diameter and depletion layer width. Theoretical scaling behavior incorporating depletion is compared to experimental results. Experimental fit parameters: A = 0.48 and ρ = 0.26, EMT fit parameters: A = 0.46 and ρ = 0.19. (b) Schematic showing how the gap:diameter ratio is adjusted to include depletion layer width in a rescaled x-axis. Rescaled plasmon ruler to account for the depletion layer as part of the gap distance. EMT fit parameters: A = 0.40 and ρ = 0.31. EMT predictions are based on a core−shell Drude dielectric function (see the Methods section in the Supporting Information). Square markers represent superlattices made from indium-doped cadmium oxide (ICO) NCs. Note the larger decay constant reflects fitting to the wider rescaled x-axis (see also Figure S11 and Table S5). Both insets show semilogarithmic plots.

metal nanoparticles[49,50] to ITO NC superlattices. The experimental shifts for the doping series are again well reproduced by EMT (Figure 2f and Figure S7), indicating that HEDA fitting and GISAXS are effectively capturing the single-NC and assembly structural attributes that govern the spectral shifts in the superlattices.

To go beyond a qualitative assessment of coupling trends, we plotted our results according to the typical plasmon ruler form, i.e., scaled spectral shift vs scaled spacing. By rescaling the frequency to the initial LSPR frequency ω_0, the relative shifts are seen to increase with both size and % Sn (Figure S9). These normalized frequency shifts are plotted against the gap:NC diameter ratio to compare to scaling expectations based on the plasmon ruler concept (Figure 3a). The data from the size series could be fit to an exponential decay, while the doping series points are closely clustered along the x-axis, having been synthesized with nearly identical sizes. For comparison to the size series, EMT was used to predict the scaling behavior of nanoparticles with a generic metallic dielectric function (i.e., Drude model with constant damping) over the same range, employing a packing fraction consistent with the experimental GISAXS data (see the Methods section in the Supporting Information). While experimental film thicknesses vary, a constant film thickness of 300 nm (close to the average of the experiments) was chosen for these (and subsequent) calculations to isolate the trends of interest. From finite element method COMSOL simulations, we observe that, while film thickness impacts extinction magnitudes, it only modestly affects CPR peak frequencies, validating this approximation for evaluating trends in peak frequencies (Figures S4 and S5). To evaluate the extent to which this simple model effectively predicts the size-scaling of LSPR coupling in our ITO NC superlattices, we fit both the experimental size series and EMT predictions with exponential functions, $y = Ae^{-x/\rho}$, where $y = \Delta\omega/\omega_0$, x is the gap:NC diameter ratio, A is a constant representing the maximum magnitude of the frequency shift, and ρ is the coupling decay parameter. The decay length, ρ, was 0.26 for the experimental data and 0.27 for the EMT predictions, both greater than the value of 0.22 found by fitting the theoretical plasmon ruler for an isolated pair of particles over the same range of scaled spacing (Figure S10). In the literature on noble-metal nanoparticles, superlattice plasmon rulers have also been reported to exhibit larger decay constants (0.4−0.6)[65,66] than those of isolated nanoparticle pairs (0.14−0.22),[11,67−70] though the values depend significantly on the range of gap/diameter values considered. Still, the general trend indicates a slower decay of coupling in more extended assemblies with more neighboring particles coupling to each particle's LSPR.

The predicted scaling with Drude-like nanoparticles is a good match for the experimental results for the ITO NC size series (Figure 3a), but it cannot explain the variation in scaled spectral shift with % Sn. The experiments show that higher % Sn increases the relative plasmon shift, even as scaled spacing is approximately constant; these data points are predicted theoretically to collapse to a single point on the plasmon ruler scaling relationship (Figure 3a). We hypothesized that the unaccounted-for variation in coupling with dopant concentration could be explained by the influence of variable % Sn beyond the direct effect of shifting the LSPR. Specifically, we suspected that dopant-driven changes in the width of the surface depletion layer, which is known to affect LSPR response in ITO NCs,[29,34,71] could be responsible for the

https://doi.org/10.1021/acsmaterialslett.4c00220
ACS Materials Lett. 2024, 6, 1929−1937

deviations from the expected scaling of plasmon coupling in our superlattices.

The presence of a surface depletion layer in ITO NCs impacts their LSPR response by reducing the plasmonically active volume and diminishing the concentration of free electrons in the NC core.[29,35] Poisson's equation predicts that the depletion width should scale as $N_d^{-1/2}$, where N_d is the concentration of donor defects, and—based on HEDA analysis of dispersed ITO NCs—the depletion layer thickness decreases as % Sn increases.[29,35,72] We hypothesize that the depletion layer could be affecting plasmon coupling strength in the ITO NC superlattices, where, in conjunction with the electron concentration, Sn doping is also modulating the depletion layer. The depletion layer acts as an additional dielectric spacer between the plasmonic cores of the NCs, reducing spectral shifts due to plasmon coupling.[73] The presence of the depletion layer and its systematic dependence on % Sn, may explain the differences between experimental and EMT-predicted (generic Drude model) scaling trends. These differences are highlighted by plotting the relative plasmon shift, since it depends on % Sn. The normalized shift is observed to increase systematically while EMT with a generic Drude model predicts it should be nearly invariant (Figure 3b). To investigate if depletion can rationalize the dopant dependence of plasmon coupling in these ITO NC superlattices, we return to the core−shell dielectric function used in Figure 2 to compute revised scaling predictions using EMT.

Simply introducing a model depletion layer into the EMT predictions provides a poor description of the experimental scaling behavior (Figure 4a). The shorter decay range, ρ, reflects that LSPR coupling falls off more rapidly for plasmonic nanoparticles with a depletion layer, which is conceptually consistent with having a smaller effective (plasmonic core) diameter. Unlike the generic Drude model, the core−shell model can be used to predict spectral shifts for variable % Sn in identically sized NCs. However, these points are offset vertically from the size-scaling relationship for a single dopant concentration (Figure 4a), so this approach fails to provide a unified description of plasmon coupling-induced shifts. The predictions also systematically underestimate the magnitude of the plasmon shifts observed experimentally. To address these limitations, we propose that the spacing between the NCs can be conceptualized as a sum of two contributions: the physical gap controlled by the ligand shell and an additional electronic gap introduced by the depletion layer (Figure 4b). To evaluate how plasmon coupling scales with this overall gap distance, we evaluate a dopant-dependent plasmon ruler that incorporates a variable depletion layer in distance scaling.

To account for the variation in the depletion layer with % Sn, we rescaled the x-axis of the plasmon ruler to include the depletion layer as part of the gap distance and to replace the physical NC diameter with the estimated plasmonic core size. However, since the depletion layer has a higher dielectric constant than the ligands between the NCs, we multiply the depletion width (W) by a dielectric screening ratio of ϵ_m/ϵ_s, where ϵ_m is the dielectric constant for the ligand shell (ϵ_m = 2.13), and ϵ_s is the dielectric constant for In_2O_3 (ϵ_s = 4), to account for the differences in screening in the two components of the redefined "gap". Approximating the dielectric constant of the depletion layer as the high-frequency dielectric constant is consistent with the core−shell model we employed (Figure 4b). For the predicted scaling relationship, NC diameters from 10 nm to 30 nm (at an N_d of 8.2×10^{20} cm^{-3}, corresponding to the average electron concentration of the experimental size series) and a range of N_d from 7×10^{19} to 1×10^{21} cm^{-3} (with 10.9 nm diameter, corresponding to the average diameter of the experimental doping series, and to % Sn of 0.5 to 5 if the dopants were fully ionized) were considered. Over this range, the theoretical depletion width varies between 0.5 and 2.5 nm, which approximately encompasses the experimental range probed. The resulting points fit on a single curve relating the scaled spectral shift to the renormalized gap distance. Once the dielectric screening and renormalizing of the core and gap sizes are taken into account, the parameters of this depletion-informed plasmon ruler scaling are nearly identical to those of the conventional plasmon ruler found when considering only physical dimensions for assemblies of Drude-like nanoparticles (Figure 3a and Table S5).

To map the experimental data points onto this renormalized x-axis, the depletion layer widths (times 2) found by HEDA fitting[29] were subtracted from the NC diameter to yield the diameter of the plasmonic core, and multiplied by the dielectric screening ratio (ϵ_m/ϵ_s) then added to the gap distance to give the effective overall gap distance (Table S2). For the size series, the depletion width is expected to be approximately constant; therefore, the average depletion width (0.19 nm) was used in the analysis to reduce uncertainty in the values. For the doping series, the depletion width varies with % Sn, so the depletion layer widths found by HEDA for each sample were used to adjust their gap:diameter ratios individually. The experimental data points across both the size and doping series approximately agree with the rescaled predicted behavior except for the two lowest dopant concentrations where the estimated volume fraction of the plasmonic core is less than half of the NC's physical volume (Figure 4b). Under these conditions, the band bending is extreme throughout the NC volume[34,36,71] and the model of a core with constant electron concentration surrounded by a fully depleted shell becomes a poorer approximation, whereas thinking of the depletion layer as a gradient of decaying electron concentration would be a better representation of the wide depletion layer in these lower doped samples. Although the rescaled plasmon ruler qualitatively captures the dopant-dependent scaling of spectral shifts, these low-doped NCs retain stronger coupling than predicted, as reflected in their relative shifts lying well above the predicted scaling relationship, where the depletion layer is treated as a purely dielectric shell.

To test the applicability of this concept to other materials known to have depletion layers, we placed data points for superlattices of indium-doped cadmium oxide (ICO) NCs on the rescaled plasmon ruler (Figure 4b).[36,74] Using ICO NCs with varying sizes and indium doping concentrations and with the same oleate surface ligands, superlattices were assembled by a similar evaporation process and found to have the same FCC packing order. Complete characterization of these samples can be found in a recent investigation into the surface depletion layer effects in ICO NCs.[75] To map these samples onto the rescaled ruler, the average gap distance of 3.17 nm, their experimentally determined depletion layer widths from HEDA analysis, and the dielectric constant for CdO (ϵ_s = 5.5) were used. These data points follow the same coupling trends as ITO NCs, where larger diameters or higher doping concentrations lead to stronger coupling. We see in the rescaled plasmon ruler that samples with wider depletion layers

https://doi.org/10.1021/acsmaterialslett.4c00220
ACS Materials Lett. 2024, 6, 1929−1937

(lower In doping %) display a steeper decay in coupling strength with increasing effective gap distance (Figure 4b). This data serves as a preliminary indication that the rescaling proposed here could provide a broadly applicable rationalization of how the coupling between assembled plasmonic metal-oxide NCs is affected by the presence of depletion layers.

In conclusion, we have evaluated the structure- and composition-dependent plasmon coupling in ITO NC superlattices by quantifying spectral shifts for a library of NCs with varied sizes and Sn dopant concentrations. Higher % Sn enhances coupling, resulting in a dopant dependence of the spectral redshift upon assembly that remains even when normalized by the LSPR frequency of the dispersed NCs. We attribute this deviation from conventional plasmon ruler behavior to the surface depletion layer, whose width depends systematically on the dopant concentration. We propose rescaling of the gap and plasmonic diameter to approximately account for the depletion layer and its dielectric environment, which allows spectral shifts in assemblies of NCs with varying dopant concentrations to be described and predicted by a single, broadly applicable scaling law. Although the spectral shifts of experimental assemblies with the most substantial depletion layers (i.e., the lowest % Sn) are larger than predicted by this rescaled plasmon ruler, it may still serve as a useful empirical guide to designing materials with targeted spectral features. Further refinement of the elaborated model might be made by going beyond a simple core−shell model for the surface-depleted NCs, for example by approximating the electron distribution with multiple shells of progressively lower electron concentration approaching the surface.[34,36]

The importance of depletion layers in modulating plasmon shifts upon assembly suggests novel ways to design functional materials not available with noble-metal nanoparticles. Understanding depletion layer effects on coupling, as established in this work, can be expanded to quantitatively describe coupling in assemblies of other doped metal-oxide NCs, such as indium-doped cadmium oxide.[36,74,75] Besides dopant concentration, depletion layer width can be tuned by the dipoles of surface capping ligands or by varying the radial distribution of dopants.[72,76] Combining depletion layer control with NC spacing and the overall density and architecture of the assemblies,[6,77] a multifaceted materials design space is unveiled for creating photonic materials with desirable spectral features and near-field hot spots. Ultimately, the ability to engineer NC assemblies with targeted properties will enable the efficient design of functional plasmonic materials, accelerating discovery for new technologies.

■ ASSOCIATED CONTENT

Supporting Information

The Supporting Information is available free of charge at https://pubs.acs.org/doi/10.1021/acsmaterialslett.4c00220.

All experimental methods in detail, full materials characterization including microscopy images and GI-(SAXS) of each NC sample, and full theoretical methods, including all modeling of the experimental dataset (PDF)

■ AUTHOR INFORMATION

Corresponding Authors

Thomas M. Truskett − *McKetta Department of Chemical Engineering, University of Texas at Austin, Austin, Texas 78712, United States; Department of Physics, University of Texas at Austin, Austin, Texas 78712, United States*; Email: truskett@che.utexas.edu

Delia J. Milliron − *McKetta Department of Chemical Engineering and Department of Chemistry, University of Texas at Austin, Austin, Texas 78712, United States*; Email: milliron@che.utexas.edu

Authors

M. Wren Berry − *Department of Chemistry, University of Texas at Austin, Austin, Texas 78712, United States*

Allison M. Green − *McKetta Department of Chemical Engineering, University of Texas at Austin, Austin, Texas 78712, United States*

Benjamin J. Roman − *McKetta Department of Chemical Engineering, University of Texas at Austin, Austin, Texas 78712, United States*

Complete contact information is available at: https://pubs.acs.org/10.1021/acsmaterialslett.4c00220

Notes

The authors declare no competing financial interest.

■ ACKNOWLEDGMENTS

This work was primarily supported by the National Science Foundation through the Center for Dynamics and Control of Materials: an NSF Materials Research Science and Engineering Center (NSF MRSEC) under Cooperative Agreement Nos. DMR-1720595 and DMR-2308817. This work was also supported by the Welch Foundation (Nos. F-1848 and F-1696) and by NSF Grant No. CHE-2303296. SAXS data was collected at UT Austin with an instrument acquired under NSF MRI grant (No. CBET-1624659). The authors thank Drs. Manuel Dominguez and Ankit Agrawal for contributing to the conception of this project. The authors also thank Sofia Shubert-Zuleta, Victor Segui Barragan, and Dr. Daniel Davies for their guidance and helpful discussions, as well as Dr. Woo Je Chang for his preliminary data during the revision process.

■ REFERENCES

(1) Collier, C.; Vossmeyer, T.; Heath, J. Nanocrystal superlattices. *Annu. Rev. Phys. Chem.* **1998**, *49*, 371−404.

(2) Talapin, D. V.; Lee, J.-S.; Kovalenko, M. V.; Shevchenko, E. V. Prospects of colloidal nanocrystals for electronic and optoelectronic applications. *Chem. Rev.* **2010**, *110*, 389−458.

(3) Tao, A. R.; Ceperley, D. P.; Sinsermsuksakul, P.; Neureuther, A. R.; Yang, P. Self-organized silver nanoparticles for three-dimensional plasmonic crystals. *Nano Lett.* **2008**, *8*, 4033−4038.

(4) Hutter, E.; Fendler, J. H. Exploitation of localized surface plasmon resonance. *Adv. Mater.* **2004**, *16*, 1685−1706.

(5) Agrawal, A.; Cho, S. H.; Zandi, O.; Ghosh, S.; Johns, R. W.; Milliron, D. J. Localized surface plasmon resonance in semiconductor nanocrystals. *Chem. Rev.* **2018**, *118*, 3121−3207.

(6) Chen, C.-F.; Tzeng, S.-D.; Chen, H.-Y.; Lin, K.-J.; Gwo, S. Tunable plasmonic response from alkanethiolate-stabilized gold nanoparticle superlattices: evidence of near-field coupling. *J. Am. Chem. Soc.* **2008**, *130*, 824−826.

(7) Ghosh, S. K.; Pal, T. Interparticle coupling effect on the surface plasmon resonance of gold nanoparticles: From theory to applications. *Chem. Rev.* **2007**, *107*, 4797−4862.

(8) Jain, P. K.; El-Sayed, M. A. Plasmonic coupling in noble metal nanostructures. *Chem. Phys. Lett.* **2010**, *487*, 153−164.

(9) Nordlander, P.; Oubre, C.; Prodan, E.; Li, K.; Stockman, M. Plasmon hybridization in nanoparticle dimers. *Nano Lett.* **2004**, *4*, 899−903.

(10) Prodan, E.; Radloff, C.; Halas, N. J.; Nordlander, P. A hybridization model for the plasmon response of complex nanostructures. *Science* **2003**, *302*, 419−422.
(11) Jain, P. K.; Huang, W.; El-Sayed, M. A. On the universal scaling behavior of the distance decay of plasmon coupling in metal nanoparticle pairs: A plasmon ruler equation. *Nano Lett.* **2007**, *7*, 2080−2088.
(12) Funston, A. M.; Novo, C.; Davis, T. J.; Mulvaney, P. Plasmon coupling of gold nanorods at short distances and in different geometries. *Nano Lett.* **2009**, *9*, 1651−1658.
(13) Su, K.-H.; Wei, Q.-H.; Zhang, X.; Mock, J.; Smith, D. R.; Schultz, S. Interparticle coupling effects on plasmon resonances of nanogold particles. *Nano Lett.* **2003**, *3*, 1087−1090.
(14) Rechberger, W.; Hohenau, A.; Leitner, A.; Krenn, J.; Lamprecht, B.; Aussenegg, F. Optical properties of two interacting gold nanoparticles. *Opt. Commun.* **2003**, *220*, 137−141.
(15) Sönnichsen, C.; Reinhard, B. M.; Liphardt, J.; Alivisatos, A. P. A molecular ruler based on plasmon coupling of single gold and silver nanoparticles. *Nat. Biotechnol.* **2005**, *23*, 741−745.
(16) Wang, Y.; Yang, Z.; Wei, J. Surface plasmon resonance properties of silver nanocrystal superlattices spaced by polystyrene ligands. *J. Phys. Chem. C* **2022**, *126*, 4948−4958.
(17) Harfenist, S. A.; Wang, Z.; Alvarez, M. M.; Vezmar, I.; Whetten, R. L. Highly oriented molecular Ag nanocrystal arrays. *J. Phys. Chem.* **1996**, *100*, 13904−13910.
(18) Schulz, F.; Pavelka, O.; Lehmkühler, F.; Westermeier, F.; Okamura, Y.; Mueller, N. S.; Reich, S.; Lange, H. Structural order in plasmonic superlattices. *Nat. Commun.* **2020**, *11*, 3821.
(19) Lu, B.; Vegso, K.; Micky, S.; Ritz, C.; Bodik, M.; Fedoryshyn, Y. M.; Siffalovic, P.; Stemmer, A. Tunable subnanometer gaps in self-assembled monolayer gold nanoparticle superlattices enabling strong plasmonic field confinement. *ACS Nano* **2023**, *17*, 12774−12787.
(20) Green, A. M.; Chang, W. J.; Sherman, Z. M.; Sakotic, Z.; Kim, K.; Wasserman, D.; Milliron, D. J.; Truskett, T. M. Structural Order and Plasmonic Response of Nanoparticle Monolayers. *ACS Photonics* **2024**, *11*, 1280−1292.
(21) Mueller, N. S.; Pfitzner, E.; Okamura, Y.; Gordeev, G.; Kusch, P.; Lange, H.; Heberle, J.; Schulz, F.; Reich, S. Surface-enhanced Raman scattering and surface-enhanced infrared absorption by plasmon polaritons in three-dimensional nanoparticle supercrystals. *ACS Nano* **2021**, *15*, 5523−5533.
(22) Ling, L.; Zhu, R.; Gu, Y.; Chen, Z. Doped semiconductor nanoparticles for possible daytime radiative cooling applications. *Semicond. Sci. Technol.* **2020**, *35*, 075018.
(23) Agrawal, A.; Singh, A.; Yazdi, S.; Singh, A.; Ong, G. K.; Bustillo, K.; Johns, R. W.; Ringe, E.; Milliron, D. J. Resonant Coupling between Molecular Vibrations and Localized Surface Plasmon Resonance of Faceted Metal Oxide Nanocrystals. *Nano Lett.* **2017**, *17*, 2611−2620.
(24) Kim, K.; Sherman, Z. M.; Cleri, A.; Chang, W. J.; Maria, J.-P.; Truskett, T. M.; Milliron, D. J. Hierarchically Doped Plasmonic Nanocrystal Metamaterials. *Nano Lett.* **2023**, *23*, 7633−7641.
(25) Matsui, H.; Hasebe, T.; Hasuike, N.; Tabata, H. Plasmonic heat shielding in the infrared range using oxide semiconductor nanoparticles based on Sn-doped In_2O_3: effect of size and interparticle gap. *ACS Appl. Nano Mater.* **2018**, *1*, 1853−1862.
(26) Chang, W. J.; Sakotic, Z.; Ware, A.; Green, A. M.; Roman, B. J.; Kim, K.; Truskett, T. M.; Wasserman, D.; Milliron, D. J. Wavelength Tunable Infrared Perfect Absorption in Plasmonic Nanocrystal Monolayers. *ACS Nano* **2024**, *18*, 972−982.
(27) Liu, X.; Swihart, M. T. Heavily-doped colloidal semiconductor and metal oxide nanocrystals: an emerging new class of plasmonic nanomaterials. *Chem. Soc. Rev.* **2014**, *43*, 3908−3920.
(28) Staller, C. M.; Gibbs, S. L.; Saez Cabezas, C. A.; Milliron, D. J. Quantitative analysis of extinction coefficients of tin-doped indium oxide nanocrystal ensembles. *Nano Lett.* **2019**, *19*, 8149−8154.
(29) Gibbs, S. L.; Staller, C. M.; Agrawal, A.; Johns, R. W.; Saez Cabezas, C. A.; Milliron, D. J. Intrinsic optical and electronic properties from quantitative analysis of plasmonic semiconductor nanocrystal ensemble optical extinction. *J. Phys. Chem. C* **2020**, *124*, 24351−24360.
(30) Li, S. Q.; Guo, P.; Zhang, L.; Zhou, W.; Odom, T. W.; Seideman, T.; Ketterson, J. B.; Chang, R. P. Infrared plasmonics with indium-tin-oxide nanorod arrays. *ACS Nano* **2011**, *5*, 9161−9170.
(31) Li, S.-Q.; Guo, P.; Buchholz, D. B.; Zhou, W.; Hua, Y.; Odom, T. W.; Ketterson, J.; Ocola, L. E.; Sakoda, K.; Chang, R. P. Plasmonic-photonic mode coupling in indium-tin-oxide nanorod arrays. *ACS Photonics* **2014**, *1*, 163−172.
(32) Abb, M.; Wang, Y.; Papasimakis, N.; De Groot, C.; Muskens, O. L. Surface-enhanced infrared spectroscopy using metal oxide plasmonic antenna arrays. *Nano Lett.* **2014**, *14*, 346−352.
(33) Olafsson, A.; Khorasani, S.; Busche, J. A.; Araujo, J. J.; Idrobo, J. C.; Gamelin, D. R.; Masiello, D. J.; Camden, J. P. Imaging infrared plasmon hybridization in doped semiconductor nanocrystal dimers. *J. Phys. Chem. Lett.* **2021**, *12*, 10270−10276.
(34) Zandi, O.; Agrawal, A.; Shearer, A. B.; Reimnitz, L. C.; Dahlman, C. J.; Staller, C. M.; Milliron, D. J. Impacts of surface depletion on the plasmonic properties of doped semiconductor nanocrystals. *Nat. Mater.* **2018**, *17*, 710−717.
(35) Gibbs, S. L.; Staller, C. M.; Milliron, D. J. Surface depletion layers in plasmonic metal oxide nanocrystals. *Acc. Chem. Res.* **2019**, *52*, 2516−2524.
(36) Ghini, M.; Curreli, N.; Lodi, M. B.; Petrini, N.; Wang, M.; Prato, M.; Fanti, A.; Manna, L.; Kriegel, I. Control of electronic band profiles through depletion layer engineering in core-shell nanocrystals. *Nat. Commun.* **2022**, *13*, 537.
(37) Jansons, A. W.; Hutchison, J. E. Continuous growth of metal oxide nanocrystals: Enhanced control of nanocrystal size and radial dopant distribution. *ACS Nano* **2016**, *10*, 6942−6951.
(38) Ito, D.; Yokoyama, S.; Zaikova, T.; Masuko, K.; Hutchison, J. E. Synthesis of ligand-stabilized metal oxide nanocrystals and epitaxial core/shell nanocrystals via a lower-temperature esterification process. *ACS Nano* **2014**, *8*, 64−75.
(39) Ofosu, C. K.; Kang, J.; Truskett, T. M.; Milliron, D. J. Effective Hard-Sphere Repulsions between Oleate-Capped Colloidal Metal Oxide Nanocrystals. *J. Phys. Chem. Lett.* **2022**, *13*, 11323−11329.
(40) Li, C.; Liu, L.; Zhang, Z.; Zhang, D.; Yi, S.; Yang, H.; Fan, Z. Anisotropy in Near-Spherical Colloidal Nanoparticles. *ACS Nano* **2023**, *17*, 17873−17883.
(41) Shevchenko, E. V.; Talapin, D. V.; Murray, C. B.; O'Brien, S. Structural characterization of self-assembled multifunctional binary nanoparticle superlattices. *J. Am. Chem. Soc.* **2006**, *128*, 3620−3637.
(42) Shevchenko, E. V.; Talapin, D. V.; Kotov, N. A.; O'Brien, S.; Murray, C. B. Structural diversity in binary nanoparticle superlattices. *Nature* **2006**, *439*, 55−59.
(43) Jiang, Z. GIXSGUI: A MATLAB toolbox for grazing-incidence X-ray scattering data visualization and reduction, and indexing of buried three-dimensional periodic nanostructured films. *J. Appl. Crystallogr.* **2015**, *48*, 917−926.
(44) Winslow, S. W.; Swan, J. W.; Tisdale, W. A. The importance of unbound ligand in nanocrystal superlattice formation. *J. Am. Chem. Soc.* **2020**, *142*, 9675−9685.
(45) Bian, K.; Choi, J. J.; Kaushik, A.; Clancy, P.; Smilgies, D.-M.; Hanrath, T. Shape-anisotropy driven symmetry transformations in nanocrystal superlattice polymorphs. *ACS Nano* **2011**, *5*, 2815−2823.
(46) Calvin, J. J.; Brewer, A. S.; Alivisatos, A. P. The role of organic ligand shell structures in colloidal nanocrystal synthesis. *Nat. Synth.* **2022**, *1*, 127−137.
(47) Weir, M. P.; Toolan, D. T.; Kilbride, R. C.; Penfold, N. J.; Washington, A. L.; King, S. M.; Xiao, J.; Zhang, Z.; Gray, V.; Dowland, S.; Winkel, J.; Greenham, N. C.; Friend, R. H.; Rao, A.; Ryan, A. J.; Jones, R. A. Ligand shell structure in lead sulfide-oleic acid colloidal quantum dots revealed by small-angle scattering. *J. Phys. Chem. Lett.* **2019**, *10*, 4713−4719.
(48) Toolan, D. T.; Weir, M. P.; Allardice, J.; Smith, J. A.; Dowland, S. A.; Winkel, J.; Xiao, J.; Zhang, Z.; Gray, V.; Washington, A. L.; Petty, A. J. I.; Anthony, J. E.; Greenham, N. C.; Friend, R. H.; Rao, A.; Jones, R. A.; Ryan, A. J. Insights into the Structure and Self-Assembly

https://doi.org/10.1021/acsmaterialslett.4c00220
ACS Materials Lett. 2024, 6, 1929−1937

of Organic-Semiconductor/Quantum-Dot Blends. *Adv. Funct. Mater.* **2022**, *32*, 2109252.
(49) Kinnan, M. K.; Chumanov, G. Plasmon coupling in two-dimensional arrays of silver nanoparticles: II. Effect of the particle size and interparticle distance. *J. Phys. Chem. C* **2010**, *114*, 7496−7501.
(50) Chen, T.; Pourmand, M.; Feizpour, A.; Cushman, B.; Reinhard, B. M. Tailoring plasmon coupling in self-assembled one-dimensional Au nanoparticle chains through simultaneous control of size and gap separation. *J. Phys Chem. Lett.* **2013**, *4*, 2147−2152.
(51) Lounis, S. D.; Runnerstrom, E. L.; Bergerud, A.; Nordlund, D.; Milliron, D. J. Influence of dopant distribution on the plasmonic properties of indium tin oxide nanocrystals. *J. Am. Chem. Soc.* **2014**, *136*, 7110−7116.
(52) Crockett, B. M.; Jansons, A. W.; Koskela, K. M.; Johnson, D. W.; Hutchison, J. E. Radial dopant placement for tuning plasmonic properties in metal oxide nanocrystals. *ACS Nano* **2017**, *11*, 7719−7728.
(53) Tandon, B.; Yadav, A.; Khurana, D.; Reddy, P.; Santra, P. K.; Nag, A. Size-induced enhancement of carrier density, LSPR quality factor, and carrier mobility in Cr-Sn doped In_2O_3 nanocrystals. *Chem. Mater.* **2017**, *29*, 9360−9368.
(54) Wei, J.; Deeb, C.; Pelouard, J.-L.; Pileni, M.-P. Influence of cracks on the optical properties of silver nanocrystals supracrystal films. *ACS Nano* **2019**, *13*, 573−581.
(55) Sherman, Z. M.; Kim, K.; Kang, J.; Roman, B. J.; Crory, H. S.; Conrad, D. L.; Valenzuela, S. A.; Lin, E.; Dominguez, M. N.; Gibbs, S. L.; Anslyn, E. V.; Milliron, D. J.; Truskett, T. M. Plasmonic response of complex nanoparticle assemblies. *Nano Lett.* **2023**, *23*, 3030−3037.
(56) Xi, M.; Reinhard, B. M. Localized surface plasmon coupling between mid-IR-resonant ITO nanocrystals. *J. Phys. Chem. C* **2018**, *122*, 5698−5704.
(57) Niklasson, G. A.; Granqvist, C. G.; Hunderi, O. Effective medium models for the optical properties of inhomogeneous materials. *Appl. Opt.* **1981**, *20*, 26−30.
(58) Young, K. L.; Ross, M. B.; Blaber, M. G.; Rycenga, M.; Jones, M. R.; Zhang, C.; Senesi, A. J.; Lee, B.; Schatz, G. C.; Mirkin, C. A. Using DNA to design plasmonic metamaterials with tunable optical properties. *Adv. Mater.* **2014**, *26*, 653−659.
(59) Park, D. J.; Zhang, C.; Ku, J. C.; Zhou, Y.; Schatz, G. C.; Mirkin, C. A. Plasmonic photonic crystals realized through DNA-programmable assembly. *Proc. Natl. Acad. Sci. U.S.A.* **2015**, *112*, 977−981.
(60) Torquato, S. Effective electrical conductivity of two-phase disordered composite media. *J. Appl. Phys.* **1985**, *58*, 3790−3797.
(61) McPhedran, R. C.; Milton, G. W. Bounds and Exact Theories for the Transport Properties of Inhomogeneous Media. *Appl. Phys. A: Mater. Sci. Process.* **1981**, *26*, 207−220.
(62) Farbman, I.; Levi, O.; Efrima, S. Optical response of concentrated colloids of coinage metals in the near-ultraviolet, visible, and infrared regions. *J. Chem. Phys.* **1992**, *96*, 6477−6485.
(63) Maurice, M. S.; Barros, N.; Kachkachi, H. Beyond the Maxwell Garnett approximation for interacting plasmonic nanoparticles: An analytical and numerical study. *J. Appl. Phys.* **2023**, *134*, 094303.
(64) Abdul-Gader Jafar, M. M. Comprehensive formulations for the total normal-incidence optical reflectance and transmittance of thin films laid on thick substrates. *Eur. Int. J. Sci. Technol.* **2013**, *2*, 214−274.
(65) Ben, X.; Park, H. S. Size dependence of the plasmon ruler equation for two-dimensional metal nanosphere arrays. *J. Phys. Chem. C* **2011**, *115*, 15915−15926.
(66) Yockell-Lelièvre, H.; Gingras, D.; Vallée, R.; Ritcey, A. M. Coupling of localized surface plasmon resonance in self-organized polystyrene-capped gold nanoparticle films. *J. Phys. Chem. C* **2009**, *113*, 21293−21302.
(67) Tabor, C.; Murali, R.; Mahmoud, M.; El-Sayed, M. A. On the use of plasmonic nanoparticle pairs as a plasmon ruler: The dependence of the near-field dipole plasmon coupling on nanoparticle size and shape. *J. Phys. Chem. A* **2009**, *113*, 1946−1953.
(68) Maye, M. M.; Nykypanchuk, D.; Cuisinier, M.; Van Der Lelie, D.; Gang, O. Stepwise surface encoding for high-throughput assembly of nanoclusters. *Nat. Mater.* **2009**, *8*, 388−391.
(69) Kadkhodazadeh, S.; de Lasson, J. R.; Beleggia, M.; Kneipp, H.; Wagner, J. B.; Kneipp, K. Scaling of the surface plasmon resonance in gold and silver dimers probed by EELS. *J. Phys. Chem. C* **2014**, *118*, 5478−5485.
(70) Dolinnyi, A. I. Nanometric rulers based on plasmon coupling in pairs of gold nanoparticles. *J. Phys. Chem. C* **2015**, *119*, 4990−5001.
(71) Agrawal, A.; Kriegel, I.; Runnerstrom, E. L.; Scotognella, F.; Llordes, A.; Milliron, D. J. Rationalizing the impact of surface depletion on electrochemical modulation of plasmon resonance absorption in metal oxide nanocrystals. *ACS Photonics* **2018**, *5*, 2044−2050.
(72) Staller, C. M.; Robinson, Z. L.; Agrawal, A.; Gibbs, S. L.; Greenberg, B. L.; Lounis, S. D.; Kortshagen, U. R.; Milliron, D. J. Tuning nanocrystal surface depletion by controlling dopant distribution as a route toward enhanced film conductivity. *Nano Lett.* **2018**, *18*, 2870−2878.
(73) Tandon, B.; Agrawal, A.; Heo, S.; Milliron, D. J. Competition between depletion effects and coupling in the plasmon modulation of doped metal oxide nanocrystals. *Nano Lett.* **2019**, *19*, 2012−2019.
(74) Diroll, B. T.; Gordon, T. R.; Gaulding, E. A.; Klein, D. R.; Paik, T.; Yun, H. J.; Goodwin, E.; Damodhar, D.; Kagan, C. R.; Murray, C. B. Synthesis of N-type plasmonic oxide nanocrystals and the optical and electrical characterization of their transparent conducting films. *Chem. Mater.* **2014**, *26*, 4579−4588.
(75) Shubert-Zuleta, S. A.; Segui Barragan, V.; Berry, M. W.; Russum, R.; Milliron, D. J. How Depletion Layers Govern the Dynamic Plasmonic Response of In-doped CdO Nanocrystals. *ChemRxiv* **2024**, DOI: 10.26434/chemrxiv-2024-sfw0j
(76) Segui Barragan, V.; Roman, B. J.; Shubert-Zuleta, S. A.; Berry, M. W.; Celio, H.; Milliron, D. J. Dipolar ligands tune plasmonic properties of tin-doped indium oxide nanocrystals. *Nano Lett.* **2023**, *23*, 7983−7989.
(77) Kang, J.; Sherman, Z. M.; Conrad, D. L.; Crory, H. S.; Dominguez, M. N.; Valenzuela, S. A.; Anslyn, E. V.; Truskett, T. M.; Milliron, D. J. Structural control of plasmon resonance in molecularly linked metal oxide nanocrystal gel assemblies. *ACS Nano* **2023**, *17*, 24218−24226.

https://doi.org/10.1021/acsmaterialslett.4c00220
ACS Materials Lett. 2024, 6, 1929−1937